The 9th European Congress on Computational Methods in Applied Sciences and Engineering
ECCOMAS Congress 2024
3–7 June 2024, Lisboa, Portugal

OBJECT-BASED FULL WAVEFORM INVERSION WITH QUANTIFIED UNCERTAINTY IN STRATIFIED MEDIA

CAROLINA ABUGATTAS[1], ANA CARPIO[1], ELENA CEBRIAN[2] AND GERARDO OLEAGA[1]

[1] Departamento de Matemática Aplicada
Universidad Complutense de Madrid
Plaza de Ciencias, 28040 Madrid, Spain
e-mail: cabugatt@ucm.es, acarpio@ucm.es, goleaga@ucm.es

[2] Departamento de Matemáticas y Computación
Universidad de Burgos
Campus Milanera, C/ Villadiego s/n 09001 Burgos, Spain
e-mail: elenac@ubu.es

Key words: Computational Mechanics, FEM, Inverse Bayesian Problems, Object based full waveform inversion, Uncertainty quantification

Summary. We consider the problem of determining inclusions in layered media from noisy measurements of wave fields on the surface. For inclusions governed by a small number of parameters, we define the posterior probability of the parameter set by means of the finite dimensional Bayes's formula. We determine the maximum a posteriori approximation (MAP) of the inclusions by optimizing constrained functionals involving the measurements, the available a priori information and parameter dependent solutions of wave equation constraints with changing discontinuities which we approximate with adaptive finite element meshes. A Laplace approximation of the posterior probability about the MAP point provides basic uncertainty estimates. Markov Chain Monte Carlo (MCMC) studies allow us to quantify uncertainty in the distribution of inclusion parameters in more detail, including multimodality and asymmetry effects. However, the higher computational cost of this approach forces the use of coarse solvers defined in prefixed meshes. While we find reasonable agreement between the MAP estimates obtained in both ways, MCMC sampling unveils multimodal distributions affected by the prior knowledge and the noise to signal ratio.

1 INTRODUCTION

Noninvasive imaging techniques to study the subsurface of Earth often resort to elastic waves generated by man-made vibrations or explosions [11]. Figure 1 illustrates a typical imaging set-up. A grid of equispaced sources emits waves that propagate under the surface, interact with the structures encountered, are reflected and recorded at a grid of receivers located on the surface. Full waveform inversion techniques exploit the entire content of the recorded waves to extract parameters characterizing unknown properties of the medium [13]. Here, we assume we have characterized a basic layered structure by other techniques, for instance, classical seismic reflection or depth migration [11, 12]. Our goal is to refine the characterization of localized inclusions of different materials in the layers with quantified uncertainty. A variety of deterministic

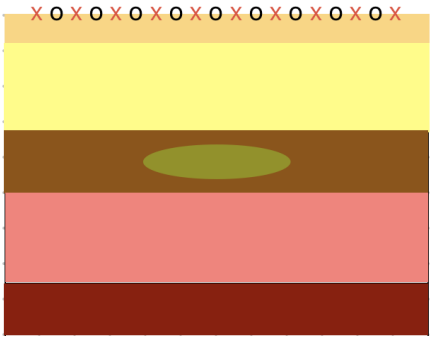

Figure 1: Schematic visualization of the imaging set-up. Circles represent sources while crosses represent receivers where wave signals are recorded.

approaches can be employed to approximate such inclusions [4, 6, 8], resorting to optimization of constrained cost functionals with total variation, Tikhonov or iterative Gauss-Newton regularizations. To quantify uncertainty we devise a finite dimensional Bayesian inverse formulation, assuming that the inclusions are characterized by a few parameters representing their material constants and geometry [2]. In our context, this approach is simpler than high dimensional Bayesian formulations [12] aiming to characterize the wave speed of each point of a mesh covering the whole region under study. It allows us to resort to FEM techniques using either adaptive or fixed meshes and investigate the influence of the choice on the results.

2 OBSERVATION OPERATOR

Measurements are related to a mathematical model of wave propagation through an observation operator. We consider a scalar model of longitudinal wave propagation

$$\begin{aligned} &\rho_{\boldsymbol{\nu}}(\mathbf{x})\, u_{tt} = \mathrm{div}[(\lambda_{\boldsymbol{\nu}}(\mathbf{x}) + 2\mu_{\boldsymbol{\nu}}(\mathbf{x}))\nabla u] + \rho(\mathbf{x}) f, && \mathbf{x} \in R,\ t > 0, \\ &\nabla u \cdot \mathbf{n} = 0, && \mathbf{x} \in \Sigma,\ t > 0, \\ &u(0,\mathbf{x}) = 0,\ u_t(0,\mathbf{x}) = 0, && \mathbf{x} \in R, \end{aligned} \tag{1}$$

where u represents the displacement generated by the force f induced by the source points. R represents the layered subsurface and Σ the upper surface where sources are located. The layered region R contains inclusions $\Omega_{\boldsymbol{\nu}}$ defined by parameter sets $\boldsymbol{\nu}$, which modify the local properties of densities and elastic constants:

$$\rho_{\boldsymbol{\nu}} = \begin{cases} \rho, & \mathbf{x} \in R \setminus \overline{\Omega_{\boldsymbol{\nu}}}, \\ \rho_{\mathrm{i}}, & \mathbf{x} \in \Omega_{\boldsymbol{\nu}}, \end{cases} \tag{2}$$

$$v_{\boldsymbol{\nu}} = \begin{cases} v, & \mathbf{x} \in R \setminus \overline{\Omega_{\boldsymbol{\nu}}}, \\ v_{\mathrm{i}}, & \mathbf{x} \in \Omega_{\boldsymbol{\nu}}, \end{cases} \tag{3}$$

where the local wave speed v is related to the elastic constants and the density by $(\lambda + 2\mu) = \rho v^2$. The observation operator assigns to each inclusion the value of the solution $u_{\boldsymbol{\nu}}$ of (1)-(3) measured at the receivers $\mathbf{r}_j$, $j = 1, \ldots, J$, during a sequence of times t_m, $m = 1, \ldots, M$:

$$\begin{aligned} \mathbf{U}: \ & \mathbb{R}^P \longrightarrow \mathbb{R}^D \\ & \boldsymbol{\nu} \longrightarrow (u_{\boldsymbol{\nu}}(\mathbf{r}_j, t_m))_{j=1,\ldots,J, m=1,\ldots,M}. \end{aligned} \tag{4}$$

Notice that we can define the value of $u_{\boldsymbol{\nu}}$ at specific points only when the solution $u_{\boldsymbol{\nu}}$ of (1-3) is smooth enough, see [1] for details. Otherwise, we need to consider alternative observation operators.

If $\boldsymbol{\nu}_{\text{true}}$ are the true parameters defining an observed inclusion, we expect the measurements to be related to the synthetically observed values

$$\mathbf{d} = \mathbf{U}(\boldsymbol{\nu}_{\text{true}}) + \boldsymbol{\eta}, \tag{5}$$

where $\boldsymbol{\eta}$ represents a random Gaussian noise term with covariance $\boldsymbol{\Gamma}_{\text{n}}$.

3 BAYESIAN INVERSE PROBLEM

Given inclusions characterized by parameters $\boldsymbol{\nu} = (\nu_1, \ldots, \nu_M)$ and measurements $\mathbf{d}$, the posterior probability density $p(\boldsymbol{\nu}|\mathbf{d})$ of having an inclusion defined by parameters $\boldsymbol{\nu}$ given data $\mathbf{d}$ is characterized by Bayes's theorem [9]

$$p_{\text{pt}}(\boldsymbol{\nu}|\mathbf{d}) = p(\mathbf{d}|\boldsymbol{\nu})\frac{p_{\text{pr}}(\boldsymbol{\nu})}{p(\mathbf{d})}, \tag{6}$$

where $p_{\text{pr}}(\boldsymbol{\nu})$ is the prior density of the parameters (which embodies expert knowledge on them) and $p(\mathbf{d}|\boldsymbol{\nu})$ is the conditional probability (or likelihood) of recording measurements $\mathbf{d}$ given parameters $\boldsymbol{\nu}$. The density $p(\mathbf{d})$ is a normalizing factor. The posterior density $p_{\text{pt}}(\boldsymbol{\nu}|\mathbf{d})$ itself is the solution of the inverse Bayesian problem.

For the specific problem under study, we define prior densities and likelihoods as follows:

$$p_{\text{pr}}(\boldsymbol{\nu}) = C\begin{cases} \frac{1}{(2\pi)^{P/2}}\frac{1}{\sqrt{|\boldsymbol{\Gamma}_{\text{pr}}|}}\exp\left(-\frac{1}{2}(\boldsymbol{\nu}-\boldsymbol{\nu}_0)^t\boldsymbol{\Gamma}_{\text{pr}}^{-1}(\boldsymbol{\nu}-\boldsymbol{\nu}_0)\right), & \boldsymbol{\nu}\in\mathcal{P}, \\ 0, & \boldsymbol{\nu}\notin\mathcal{P}, \end{cases} \tag{7}$$

$$p(\mathbf{d}|\boldsymbol{\nu}) = \frac{1}{(2\pi)^{D/2}\sqrt{|\boldsymbol{\Gamma}_{\text{n}}|}}\exp\left(-\frac{1}{2}(\mathbf{U}(\boldsymbol{\nu})-\mathbf{d})^t\boldsymbol{\Gamma}_{\text{n}}^{-1}(\mathbf{U}(\boldsymbol{\nu})-\mathbf{d})\right), \tag{8}$$

where ^{t} denotes transpose. The set $\mathcal{P}$ includes constraints on the parameters $\boldsymbol{\nu}$. We fix $P = \text{length}(\boldsymbol{\nu})$ and $D = \text{length}(\mathbf{d})$. $C > 0$ is a normalization constant. The vector $\boldsymbol{\nu}_0$ and the matrix $\boldsymbol{\Gamma}_{\text{pr}}$ represent the mean and the covariance for the prior distribution, while $\boldsymbol{\Gamma}_{\text{n}}$ is the covariance matrix for the likelihood and $\mathbf{U}(\boldsymbol{\nu})$ stands for the observation operator associated to the propagation model (1)-(3).

The full characterization of a posterior probability is a challenging task. Preliminary information is obtained from the set of parameters $\boldsymbol{\nu}_{\text{map}}$ at which the posterior probability (6) attains a global maximum, the so-called MAP (maximum a posteriori) estimate. Scaling out normalizing constants, the posterior probability to be maximized is

$$p_{\text{pt}}(\boldsymbol{\nu}|\mathbf{d}) \sim \exp\left(-\frac{1}{2}(\boldsymbol{\nu}-\boldsymbol{\nu}_0)^t\boldsymbol{\Gamma}_{\text{pr}}^{-1}(\boldsymbol{\nu}-\boldsymbol{\nu}_0) - \frac{1}{2}(\mathbf{U}(\boldsymbol{\nu})-\mathbf{d})^t\boldsymbol{\Gamma}_{\text{n}}^{-1}(\mathbf{U}(\boldsymbol{\nu})-\mathbf{d})\right) \tag{9}$$

for $\boldsymbol{\nu}\in\mathcal{P}$.

4 APPROXIMATE BAYESIAN INVERSE PROBLEM

Computational Bayesian formulations employ discretizations of the observation operator $\mathbf{U}$. We truncate the region R to obtain a bounded computational region R', on whose artificial

boundaries we enforce non-reflecting boundary conditions [5]. Since the fields $v_{\boldsymbol{\nu}}$ and $\rho_{\boldsymbol{\nu}}$ are discontinuous we resort to finite elements to approximate solutions of the resulting wave problem. Given a mesh $\mathcal{T}_{\boldsymbol{\nu}}$ adapted to the domain $\Omega_{\boldsymbol{\nu}}$ (domain decomposition) and a finite element space $V_{\boldsymbol{\nu}}^{(N)} \subset H^1(R')$, semi-discrete approximations seek $u_{\boldsymbol{\nu}}^{(N)}(t) = \sum_{n=1}^N a_n(t)\phi_{\boldsymbol{\nu},n} \in V_{\boldsymbol{\nu}}^{(N)}$ satisfying

$$\begin{aligned}\int_{R'} \rho_{\boldsymbol{\nu}}(\mathbf{x}) u_{\boldsymbol{\nu},tt}^{(N)}(\mathbf{x},t) w(\mathbf{x})\, d\mathbf{x} + \int_{R'} \rho_{\boldsymbol{\nu}}(\mathbf{x}) v_{\boldsymbol{\nu}}(\mathbf{x})^2 \nabla u_{\boldsymbol{\nu}}^{(N)}(\mathbf{x},t)\nabla w(\mathbf{x})\, d\mathbf{x} \\ + \int_{\partial R'-\Sigma} \rho_{\boldsymbol{\nu}}(\mathbf{x}) v_{\boldsymbol{\nu}}(\mathbf{x}) u_{\boldsymbol{\nu},t}^{(N)}(\mathbf{x},t)\, w(\mathbf{x})\, dS_{\mathbf{x}} = \int_{R'} \rho_{\boldsymbol{\nu}}(\mathbf{x}) f(t,\mathbf{x}) w(\mathbf{x})\, d\mathbf{x}, \\ u_{\boldsymbol{\nu}}^{(N)}(0) = u_{\boldsymbol{\nu},t}^{(N)}(0) = 0,\end{aligned} \tag{10}$$

for all $w \in V_{\boldsymbol{\nu}}^{(N)}$. Given a temporal grid $t_k = k\,\delta t$, $k = 0,\dots,K$, we the discretize the time derivatives using centered differences for $u_{\boldsymbol{\nu},tt}^{(N)}$ and backward (or centered) differences for $u_{\boldsymbol{\nu},t}^{(N)}$. We construct an approximation $u_{\boldsymbol{\nu}}^{(N),k} = \sum_{n=1}^N a_n^k \phi_{\boldsymbol{\nu},n}$, $k = 0,\dots,K$, by solving a recurrence

$$\begin{aligned}\sum_{n=1}^N B_{\boldsymbol{\nu};j,n} a_n^{k+1} = \sum_{n=1}^N B_{\boldsymbol{\nu};j,n}(2a_n^k - a_n^{k-1}) - \delta t^2 \sum_{n=1}^N C_{\boldsymbol{\nu};j,n} a_n^k \\ - \delta t \sum_{n=1}^N E_{\boldsymbol{\nu};j,n}(a_n^k - a_n^{k-1}) + \delta t^2 h_{\boldsymbol{\nu};j}^k, \quad j = 1,\dots,N,\end{aligned} \tag{11}$$

for $k \geq 1$ starting from $a_n^0 = 0$ and $a_n^1 = 0$, $n = 1,\dots,N$, see [1] for details. The step δt is chosen small enough to guarantee a CFL condition.

For simplicity, we assume that the recording times t_m are a subset of the discretization times t_k. The approximate observation operator is

$$\begin{aligned}\mathbf{U}^{\mathrm{ap}}: \ & \mathbb{R}^P \longrightarrow \mathbb{R}^D \\ & \boldsymbol{\nu} \longrightarrow (u_{\boldsymbol{\nu}}^{(N)}(\mathbf{r}_j, t_m))_{j=1,\dots,J, m=1,\dots,M}.\end{aligned} \tag{12}$$

The posterior probability under study becomes

$$p_{\mathrm{pt}}^{\mathrm{ap}}(\boldsymbol{\nu}|\mathbf{d}) \sim \exp\left(-\frac{1}{2}(\boldsymbol{\nu}-\boldsymbol{\nu}_0)^t \boldsymbol{\Gamma}_{\mathrm{pr}}^{-1}(\boldsymbol{\nu}-\boldsymbol{\nu}_0) - \frac{1}{2}(\mathbf{U}^{\mathrm{ap}}(\boldsymbol{\nu})-\mathbf{d})^t \boldsymbol{\Gamma}_{\mathrm{n}}^{-1}(\mathbf{U}^{\mathrm{ap}}(\boldsymbol{\nu})-\mathbf{d})\right) \tag{13}$$

for $\boldsymbol{\nu} \in \mathcal{P}$, zero otherwise.

5 MAXIMUM A POSTERIORI APPROXIMATION

The set of parameters $\boldsymbol{\nu}_{\mathrm{map}}^{\mathrm{ap}}$ at which the posterior distribution (13) attains a global maximum provides an approximation to the MAP point. To find $\boldsymbol{\nu}_{\mathrm{map}}^{\mathrm{ap}}$ we minimize the cost functional

$$J^{\mathrm{ap}}(\boldsymbol{\nu}) = \frac{1}{2}(\boldsymbol{\nu}-\boldsymbol{\nu}_0)^t \boldsymbol{\Gamma}_{\mathrm{pr}}^{-1}(\boldsymbol{\nu}-\boldsymbol{\nu}_0) + \frac{1}{2}(\mathbf{U}^{\mathrm{ap}}(\boldsymbol{\nu})-\mathbf{d})^t \boldsymbol{\Gamma}_{\mathrm{n}}^{-1}(\mathbf{U}^{\mathrm{ap}}(\boldsymbol{\nu})-\mathbf{d}) \tag{14}$$

when $\boldsymbol{\nu} \in \mathcal{P}$ and $\mathbf{U}^{\mathrm{ap}}(\boldsymbol{\nu})$ is the observation operator (12). The prior information encoded in $\boldsymbol{\nu}_0$ and $\boldsymbol{\Gamma}_{\mathrm{pr}}$ acts as a regularizing term with convexifying effects. We resort to iterative Levenberg-Marquardt type algorithms [10] that set $\boldsymbol{\nu}^{k+1} = \boldsymbol{\nu}^k + \boldsymbol{\xi}^{k+1}$ where $\boldsymbol{\xi}^{k+1}$ is the solution of

$$\left(\mathbf{H}(\boldsymbol{\nu}^k) + \omega_k \,\mathrm{diag}(\mathbf{H}(\boldsymbol{\nu}^k))\right)\boldsymbol{\xi}^{k+1} = -\mathbf{g}(\boldsymbol{\nu}^k), \tag{15}$$

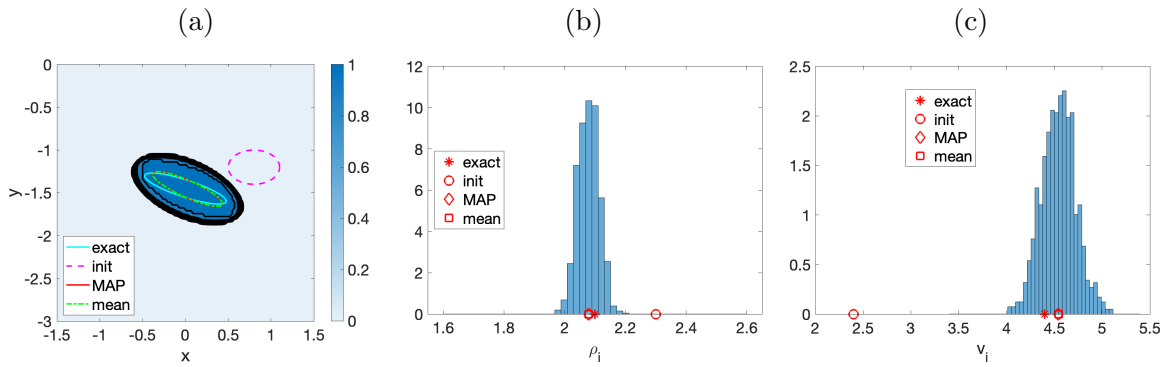

Figure 2: For the imaging set up depicted in Figure 1 and data corrupted by 10% noise: (a) MAP estimate of the inclusion shape versus true shape, (b) histograms for the density and wave speed within the inclusion, obtained by adaptive optimization and Laplace approximation.

$\mathbf{H}(\boldsymbol{\nu})$ and $\mathbf{g}(\boldsymbol{\nu})$ being the Hessian and the gradient of the cost $J^{\rm ap}(\boldsymbol{\nu})$. The small parameter $\omega_k > 0$ is adjusted to guarantee a decrease in the cost. In practice, we replace $\mathbf{H}(\boldsymbol{\nu})$ by the Gauss-Newton part of the Hessian $\mathbf{H}^{\rm GN}(\boldsymbol{\nu})$ neglecting second order derivatives. Through the optimization procedure, the inclusions $\Omega_{\boldsymbol{\nu}^k}$ considered when solving (11) to obtain $\mathbf{U}^{\rm ap}(\boldsymbol{\nu}^k)$ change. We use adaptive meshes, with elements entirely included in $\Omega_{\boldsymbol{\nu}^k}$ and $\Omega_{\boldsymbol{\nu}^k} \subset R'$, sharing vertices on $\partial\Omega_{\boldsymbol{\nu}^k}$, see [1] for details. The use of adaptive meshes allows us to resort to automatic differentiation to calculate the derivatives of the cost functional, see [1]. In simple tests, convergence is achieved in less than 50 steps.

5.1 MAP POINT BASED UNCERTAINTY ESTIMATES

Linearizing the approximate posterior density about $\boldsymbol{\nu}^{\rm ap}_{\rm map}$, we obtain a multivariate Gaussian distribution $\mathcal{N}(\boldsymbol{\nu}_{\rm map^{ap}}, \boldsymbol{\Gamma}_{\rm pt})$ approximation with covariance

$$\boldsymbol{\Gamma}_{\rm pt} = (\mathbf{F}^t \boldsymbol{\Gamma}_{\rm n}^{-1} \mathbf{F} + \boldsymbol{\Gamma}_{\rm pr}^{-1})^{-1}. \tag{16}$$

This constitutes the so-called Laplace approximation of a posterior probability [9]. We obtain basic uncertainty estimates on the true inclusion parameters drawing samples of $\mathcal{N}(\boldsymbol{\nu}_{\rm map^{ap}}, \boldsymbol{\Gamma}_{\rm pt})$ by the relation

$$\boldsymbol{\nu} = \boldsymbol{\nu}^{\rm ap}_{\rm map} + \boldsymbol{\Gamma}_{\rm pt}^{1/2} \mathbf{n}, \tag{17}$$

where $\mathbf{n}$ is a standard normal randomly generated vector (iid). Here $\mathbf{F}$ is the matrix with ℓth-column $\frac{\partial U^{\rm ap}_{\boldsymbol{\nu}}}{\partial \nu_\ell}(\mathbf{r}_j, t_n)$, $j = 1, ..., J$, $n = 1, ..., N$ evaluated at $\boldsymbol{\nu}^{\rm ap}_{\rm map}$.

Figure 2 visualizes uncertainty about inclusion parameters obtained from 10000 samples employing synthetic data generated solving (11) for the imaging set-up depicted in Figure 1 and adding 10% noise. The computational region is a rectangle of 3 Km width and 3 Km depth. We locate 51 receivers in the central part of the surface, spaced 200 m, and intercalate between them 50 sources $\mathbf{x}_j$, spaced 200 m. Each source generates a force term of the form $f_j(\mathbf{x}, t) = \frac{0.1}{(\pi\kappa)^{n/2}}(1 - 2\pi^2(f_M t)^2) e^{-\pi^2(f_M t)^2} \exp(-\frac{|\mathbf{x}-\mathbf{x}_j|^2}{10^6\kappa})$ N with $n = 2$, $\kappa = 0.04$, $f_M = 2$ Hz. The total force is the superposition of all. Adaptive FEM meshes have a minimum step 400 m. The time step for the numerical solver is 10^{-3}s. Data are recorded at the receivers each 0.1s up to a time 2.5s. Parameter values for the layered background and the true inclusion are displayed in Table 1.

Table 1: Parameter values for the imaged layered geometry

Layers	1	2	3	4	5	Inclusion	
ρ	2000	2500	2490	2490	2600	2100	kg/m^3
v	1500	2500	2800	3300	3100	4400	m/s

6 MARKOV CHAIN MONTE CARLO BASED UNCERTAINTY ESTIMATES

The unnormalized posterior distribution (13) can be directly sampled using affine invariant Markov Chain Monte Carlo samplers. Following [7], we create W chains as follows:

- Set $k=0$, $a\sim 2$ and choose number of chains W. Set sample parameter space $X=\mathbb{R}^P$.
- Draw $\boldsymbol{\nu}_1^0,\ldots,\boldsymbol{\nu}_W^0\in X$ with probability $p_{\rm pr}$.
- From $k=0$ to $k=K_{\max}$
  - Generate a permutation σ of $(1,\ldots,P)$ without fixed elements.
  - For $w=1,\ldots,W$
    - Draw z_w from $g(s)=s^{-1/2}$ if $s\in[a^{-1},a]$, 0 otherwise.
    - Set $\boldsymbol{\nu}_{\text{prop},w}=\boldsymbol{\nu}^k_{\sigma(w)}+z_w(\boldsymbol{\nu}^k_w-\boldsymbol{\nu}^k_{\sigma(w)})$.
    - Calculate the acceptance probability $\alpha=\min\left(1,z_w^{P-1}\frac{p^{\rm ap}_{\rm pt}(\boldsymbol{\nu}_{\text{prop},w})}{p^{\rm ap}_{\rm pt}(\boldsymbol{\nu}^k_w)}\right)$.
    - Draw u with uniform probability $U(0,1)$.
    - If $u<\alpha$, $\boldsymbol{\nu}^{k+1}_w=\boldsymbol{\nu}_{\text{prop},w}$, otherwise $\boldsymbol{\nu}^{k+1}_w=\boldsymbol{\nu}^k_w$.
  - Set $k=k+1$.
- Final samples from $p^{\rm ap}_{\rm pt}$: $\boldsymbol{\nu}_1^0,\boldsymbol{\nu}_2^0,\ldots,\boldsymbol{\nu}_W^0,\ \ldots,\ \boldsymbol{\nu}_1^{K_{\max}},\boldsymbol{\nu}_2^{K_{\max}},\ldots,\boldsymbol{\nu}_W^{K_{\max}}$.

This algorithm needs $W>2P$ to properly sample the target distribution and can be parallelized [3, 7]. A first block formed by B samples is discarded on account of a burn-in period. To evaluate $p^{\rm ap}_{\rm pt}$ given by (13) we need to calculate $\mathbf{U}$ap given by (12). This is done here solving (11). Typically, a few million samples may be required to properly characterize $p^{\rm ap}_{\rm pt}$. Thus, the use of adaptive meshes that change with each proposed set of parameters $\boldsymbol{\nu}^k$ is unaffordable. We are forced to employ fixed meshes $\mathcal{T}$ and finite element spaces $V^{(N)}$ for all proposed inclusions $\Omega_{\boldsymbol{\nu}^k}$, which reduces the quality of the numerical solver.

Figure 3 visualizes uncertainty about inclusion parameters obtained from 100.000 samples generated this way. Comparing to Figure 2, we observe a number of differences caused by the presence of secondary modes in addition to the main mode associated to $\boldsymbol{\nu}^{\rm ap}_{\rm map}$. The meaning of the additional modes and how we can vary the design of the imaging set-up to eliminate them deserves further study, see [1].

7 CONCLUSIONS

- Uncertainty quantification in inverse scattering problems that employ time dependent incident waves leads to solving optimization problems with time dependent wave constraints and variable discontinuities arising at the boundary of the scatterers.

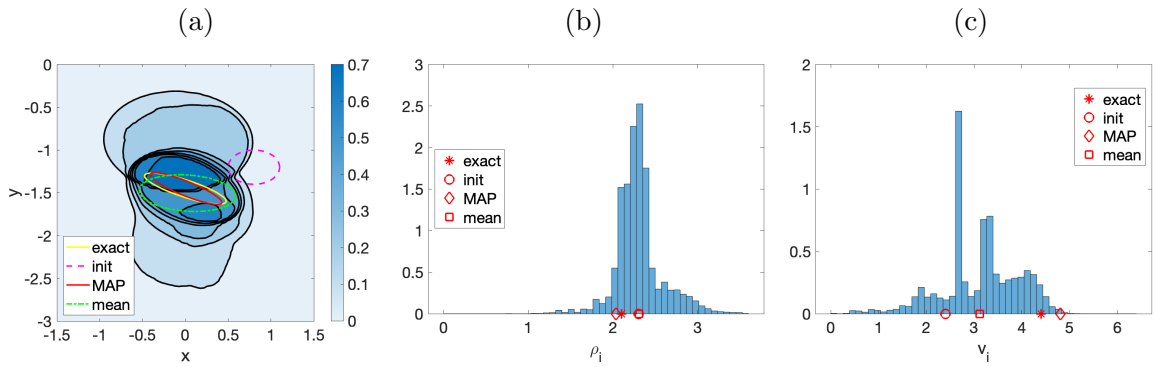

Figure 3: For the imaging set up depicted in Figure 1 and data corrupted by 10% noise: (a) MAP estimate of the inclusion shape versus true shape and contour plot of the probability of belonging to the inclusion, (b)-(c) histograms for the density and wave speed within the inclusion, obtained by MCMC sampling with a fixed FEM mesh.

- For scatterers governed by low dimensional parameter sets, adaptive FEM schemes and automatic differentiation are the basis of effective optimization approaches and basic uncertainty estimates.

- The use of detailed Markov Chain Monte Carlo samplers is possible resorting to coarse FEM solvers defined on fixed meshes, however, the interpretation of the results faces additional uncertainty due multimodality.

Acknowledgements. This research has been supported by Spanish FEDER/MICINN - AEI grant No. PID2020-112796RB-C21 and by a Doctoral Scholarship Agencia Nacional de Investigación y Desarrollo, 2022, Chile (CA).

REFERENCES

[1] Abugattas C., Carpio A., Cebrián E. and Oleaga G. 2024. "Quantifying uncertainty in inverse scattering problems set in layered geometries." Preprint

[2] Carpio A., Cebrián E. and Gutiérrez A. 2023. "Object based full waveform inversion for shear elastography." Inverse Problems 39: 075007. https://doi.org/10.1088/1361-6420/acd5f8

[3] Carpio A., Iakunin S. and Stadler G. 2020. "Bayesian approach to inverse scattering with topological priors." Inverse Problems 36: 105001. https://doi.org/10.1088/1361-6420/abaa30

[4] Carpio A., Dimiduk T.G., Le Louër F. and Rapún M.L. 2019. "When topological derivatives met regularized Gauss-Newton iterations in holographic 3D imaging". J. Comp. Phys. 388: 224-251. https://doi.org/10.1016/j.jcp.2019.03.027

[5] Engquist B. and Majda A. 1979. "Radiation boundary conditions for acoustic and elastic wave calculations". Commun. Pur. Appl. Math. 32: 312-358. https://doi.org/10.1002/cpa.3160320303

[6] Esser E., Guasch L., van Leeuwen T. and Aravkin A.Y., Herrmann F.J. 2018. "Total-variation regularization strategies in full-waveform inversion." SIAM Journal on Imaging Sciences 11: 376-406. https://doi.org/10.1137/17M111328

[7] Goodman J. and Weare J. 2010. "Ensemble samplers with affine invariance." Commun. Appl. Math. Comput. Sci. 5: 65-80. https://doi.org/10.2140/camcos.2010.5.65

[8] Guo Z. and De Hoop M.V. 2012. "Shape optimization in full waveform inversion with sparse blocky model representations'.' Proc. Proj. Rev. 1: 189-208. https://api.semanticscholar.org/CorpusID:357831

[9] MacKay D.J.C. 2003. *Information Theory, Inference and Learning Algorithms*. Cambridge University Press.

[10] Moré J.J. 1978. "The Levenberg-Marquardt Algorithm: Implementation and Theory." In Lecture Notes in Mathematics 630, edited by G. Watson. Springer.

[11] Stein S. and Wysession M. 2019. *An Introduction to Seismology, Earthquakes, and Earth Structure*, John Wiley & Sons.

[12] Zhu H., Li S., Fomel S., Stadler G. and Ghattas O. 2016. "A Bayesian approach to estimate uncertainty for full-waveform inversion using a priori information from depth migration." Geophysics 81: R307-23. https:/doi.org/10.1190/geo2015-0641.1

[13] Virieux J., Asnaashari A., Brossier R., Métivier L., Ribodetti A., and Zhou W. 2014. "6. An introduction to full waveform inversion", In Geophysical References Series: R1-1-R1-40, SEG. https://doi.org/10.1190/1.9781560803027.entry6